Determining the origin of tidal oscillations in the ionospheric transition region with EISCAT radar and global simulation data

F. Günzkofer[1], D. Pokhotelov[1], G. Stober[2], H. Liu[3], H.-L. Liu[4], N. J. Mitchell[5,6], A. Tjulin[7], and C. Borries[1]

[1]Institute for Solar-Terrestrial Physics, German Aerospace Center (DLR), Neustrelitz, Germany
[2]Institute of Applied Physics & Oeschger Center for Climate Change Research, Microwave Physics, University of Bern, Bern, Switzerland
[3]Department of Earth and Planetary Science, Kyushu University, Fukuoka, Japan
[4]High Altitude Observatory, National Center for Atmospheric Research, Boulder, CO, USA
[5]British Antarctic Survey, Cambridge, UK
[6]Department of Electronic Electrical Engineering, University of Bath, Bath, UK
[7]EISCAT Scientific Association, Kiruna, Sweden

Key Points:

- 20 day long EISCAT radar campaign shows a complex mixture of semidiurnal and diurnal tidal oscillations.
- Comparison of observational results to circulation models confirms an altitudinal two-band tidal structure, observed in the EISCAT data.
- Adaptive Spectral Filtering (ASF) technique allows to extract tidal phases, suggesting different forcings of upper and lower tidal band.

Corresponding author: Florian Günzkofer, `florian.guenzkofer@dlr.de`

Abstract

Solar and atmospheric variability influences the ionosphere, causing critical impacts on satellite and ground based infrastructure. Determining the dominant forcing mechanisms for ionosphere variability is important for prediction and mitigation of these threats. However, this is a challenging task due to the complexity of solar-terrestrial coupling processes. At high latitudes, diurnal and semidiurnal variations of temperature and neutral wind velocity can be forced from either below (lower atmosphere waves) or from above (geomagnetic and in-situ solar forcing). We analyse measurements from the incoherent scatter radar (ISR) facility operated by the European Incoherent Scatter Scientific Association (EISCAT). They are complemented by meteor radar data and compared to global circulation models. Experimental and model data both indicate the existence of strong semidiurnal oscillations in a two-band structure at altitudes $\lesssim 110$ km and $\gtrsim 130$ km, respectively. Analysis of the phase progressions suggests the upper band to be forced *in situ* while the lower band corresponds to upwards propagating tides from lower atmosphere. These results show that the actual transition of tides in the altitude region between 90 and 130 km is more complex than described so far.

1 Introduction

The ionospheric dynamo region marks the transition from a collision dominated plasma below $\sim$ 90 km to a nearly collisionless plasma above $\sim$ 150 km. Across this transition region, ion/electron gyrofrequencies $\Omega_{i/e}$ are of the same order as collision frequencies $\nu_{in/en}$. As a result, Pedersen and Hall conductivities reach their respective maxima, which in turn permits Pedersen and Hall currents perpendicular to the magnetic field. This enables global magnetospheric field-aligned current systems to be closed at these heights. However, dynamic processes in the transition region can be forced either from "above" (global plasma convection, in-situ solar irradiance absorption, auroral precipitation, etc.) or from "below" (upward propagating waves from lower atmosphere). Determining the actual forcing of specific effects in the transition region will help understanding the complex solar-terrestrial coupling processes.

One parameter to quantify the respective impact of atmospheric and solar effects are tidal-like neutral wind oscillations, especially diurnal (24 hour period) and semidiurnal (12 hour period) variations. Upward-propagating atmospheric tides of both periods are mostly forced due to ultraviolet (UV) absorption by stratospheric ozone and infrared (IR) absorption by tropospheric water vapor. The classical tidal theory (Lindzen, 1979; Andrews et al., 1987; Oberheide et al., 2011) suggests the semidiurnal atmospheric tides to dominate at latitudes above $\sim 45°$. At high latitudes, the reconnection between the Earth's magnetic field and the interplanetary magnetic field leads to a large-scale plasma convection pattern (see e.g., Kelly, 2009). This causes a predominantly 24h oscillation of zonal and meridional ion velocities which is transferred to the neutral media via ion drag and frictional heating. The transition from dominant 12h to dominant 24h oscillation regimes is observed at $\sim 115 - 120$ km altitude (Nozawa et al., 2010). However, there have been evidences for non-negligible semidiurnal oscillations as far up as ~ 250 km (R. Schunk & Nagy, 2009; Wu et al., 2017; Lee et al., 2018). Whether these 12h oscillations are signs of atmospheric tides propagating up into the ionosphere F-region or *in situ* generated oscillations remained an open question. Also, there is a general lack of continuous measurements in the region from 120 km to 250 km.

Thus, we employ two well established observation techniques to measure neutral wind velocities across the mesosphere-lower thermosphere region: meteor radars and ISR. While meteor radars are restricted in altitude coverage by meteor trail occurrence, ISR can cover the whole range from the mesopause well into the thermosphere. In this paper, we leverage the co-located Nordic Meteor Radar Network to verify the validity of the ISR measurements from EISCAT. Based on the combined neutral wind data set, we estimated 12h and 24h oscillations, considering that local measurements do not provide information on the zonal wave number to separate migrating (sun-synchronous) and non-

migrating modes from each other. Such information is taken from global model data such as Ground-to-topside model of Atmosphere and Ionosphere for Aeronomy (GAIA) and the Whole Atmosphere Community Climate Model With Thermosphere and Ionosphere Extension - Specified Dynamics (WACCM-X(SD)). The nomenclature of global tidal modes gives information on period (D: diurnal, S: semidiurnal), propagation direction (W: westward, E: eastward) as seen from an observer at a fixed geographic location on Earth and the zonal wavenumber k (Smith, 2012). While in principle the latter can take any integer value, we will restrict our analysis to $0 \leq k \leq 3$ since the by far largest amplitudes are expected for the two sun-synchronous, migrating tidal modes DW1 and SW2 (Smith, 2012).

The determination of tidal amplitudes and phases is done using the Adaptive Spectral Filtering (ASF) technique (Stober et al., 2017). Thereby, the neutral wind data in zonal and meridional direction is separately fitted for a mean background wind and several periodic components. Unless otherwise stated, amplitudes in this paper have been averaged over a sliding window of one day length. The ASF has shown to be a robust frequency analysis method for unequally spaced data (spatially and temporal). Due to the fitting of phases, the propagation of non-stationary processes (phase drifts over time) can be estimated similar to holographic analysis (Stober et al., 2020). The robustness of the fitting for short time windows enables a good resolution of the day-to-day variability of amplitudes compared to other methods. The ASF has been successfully extended and applied to fit for global tidal modes (Baumgarten & Stober, 2019; Stober et al., 2020).

The further structure of the paper is as follows. Section 2 presents the experimental setup and outlines the respective methods of neutral wind retrievals. The numerical models used to generate data are briefly introduced in Section 3. Section 4 presents the results from the analysis of measurement data and highlights the most important features, same is done for the model data in Section 5. The comparison of both as well as the interpretation and discussion are given in Section 6 and the paper is concluded in Section 7.

2 Instruments

2.1 EISCAT UHF ISR

The EISCAT Ultra High Frequency (UHF) radar at Tromsø is a powerful ISR with about 1.5-2 MW peak power on transmission operating at a frequency of 930 MHz. The system employs a dish with 32 m in diameter resulting in a beam width of about 0.7° corresponding to an antenna directive gain of approximately 48.1 dBi.

In this paper, we analyze UHF EISCAT observations collected during a campaign over more than 20 days in September 2005. This data set presents one of the longest continuous ISR measurements ever performed worldwide. More details on the experiment, data gaps, geomagnetic activity and data quality throughout the campaign are presented in Nozawa et al. (2010). Here, we make use of the existing data base. The EISCAT UHF radar in Tromsø (69.6° N, 19.2° E) (Folkestad et al., 1983) was operated in the beam swinging mode in which the radar rotates back and forth between four different pointing directions (Collis, 1995). The dwell times at the four positions and the rotation times in between result in a total time resolution of ~ 6 min. From the line of sights ion velocities measured at each pointing direction, three dimensional ion velocity vectors can be derived by inverting the radial wind equation. This is done for seven range gates corresponding to altitudes between 96 km and 142 km and one channel at ~ 300 km.

The procedure of calculating E-region neutral wind velocities $\mathbf{u}$ from ISR measurements was described in Brekke et al. (1973). It assumes a steady ion velocity $\mathbf{v}_i$ due to an equilibrium of Lorentz and ion-neutral friction force. The direct solution of the *steady state ion mobility equation* can be applied (Rino et al., 1977; Nozawa et al., 2010)

$$\mathbf{u} = \mathbf{v}_i - \frac{\Omega_i}{B\nu_{in}} \left(\mathbf{E} + \mathbf{v}_i \times \mathbf{B}\right). \tag{1}$$

As magnetic field **B**, the International Geomagnetic Reference Field (IGRF) (Barraclough, 1988) is employed. The ion gyrofrequency Ω_i is calculated from the magnetic field strength and the mean ion mass $m_i = 30.5$ amu. As suggested by Brekke et al. (1973) and demonstrated by Nozawa and Brekke (1999); Nozawa et al. (2010), the electric field **E** can be calculated at F-region region altitudes and assumed to be the same in the E-region. Since ion-neutral collisions can be neglected at higher altitudes, the ion velocity is determined by $E \times B$-drifts. The electric field is calculated as $\mathbf{E} = -\left(\mathbf{v}_{i,F} \times \mathbf{B}\right)$. F-region ion velocities $\mathbf{v}_{i,F}$ are derived from the highest altitude channel at ~ 300 km. The electric field originating from plasma convection at high latitudes quantifies the solar impact, whereas the atmospheric forcing from below strongly depends on the ion-neutral collision frequency ν_{in}, which is altitude dependent reducing the effective coupling strength with increasing thermospheric altitude. Very often collision frequencies are inferred from a model neutral atmosphere (e.g., MSIS Hedin, 1991) and a collision model which can be either empirical (Chapman, 1956) or analytical (R. W. Schunk & Walker, 1973). In this paper, we apply the NRLMSISE-00 model (Picone et al., 2002) and the empirical model for ion-neutral collision frequencies

$$\nu_{in} = 2.6 \cdot 10^{-9} \cdot n_n \left[\mathrm{cm}^{-3}\right] \cdot A^{-1/2} \ \left[\mathrm{s}^{-1}\right] \tag{2}$$

described in Chapman (1956); Kelly (2009), with neutral particle density n_n and $A = m_i$ [amu]. However, the accuracy of any collision model at altitudes $\gtrsim$ 120 km has to be considered carefully (Nozawa et al., 2010; Williams & Virdi, 1989). A direct measurement of the ion-neutral collision frequencies is possible with the current EISCAT system due to its multifrequency capability with simultaneous operation of UHF and VHF radars (Grassmann, 1993; Nicolls et al., 2014). Unfortunately, there were no multifrequency experiments scheduled during the investigated campaign and the analysis of these requires careful additional testing which is beyond the scope of this paper.

2.2 Meteor radar

Meteor radars have become an ubiquitous sensor monitoring winds at the mesosphere and lower thermosphere. These instruments observe small meteoroids, which are formed when extraterrestrial particles with a sufficient kinetic energy enter the Earth's atmosphere. Small meteoroids can penetrate deep into the atmosphere until they encounter a sufficiently dense region. The impinging atmospheric molecules and atoms decelerate and heat the particles to such an extend that the meteoric material is vaporized and atoms are released from the meteoroid. Due to the collisions with the ambient neutral atmosphere the released atoms are thermalized and form an ambipolar diffusing plasma trail, often called meteor, that is drifted by the neutral winds. Specular meteor radars detect most of these trails at altitudes between 70-110 km. For a large enough number of meteor trails, horizontal wind velocities can be measured with an 'all-sky'-fit (Hocking et al., 2001). This is usually done with a time resolution of 1h and 2 km altitude bins.

In Kiruna (67.9° N, 21.1° E), a meteor radar has been continuously operated since 1999 and therefore provides measurement for the time of the EISCAT campaign described above. Meteor radars have been used for the investigation of various types of waves in the upper atmosphere, including atmospheric tides, and provide a well tested measurement method (Pokhotelov et al., 2018; Stober et al., 2021). Since the derivation of neutral wind velocities from EISCAT measurements is not as well established, meteor radar measurements can be used as a reference at the lower boundary. In this paper, measurements from EISCAT and the Kiruna meteor radar will be merged to test the validity of the procedure described in the previous section. A large offset of ISR and meteor radar

data would be clearly visible if present. Also, the total observed altitude range is extended significantly downwards.

3 Models

3.1 GAIA

The Ground-to-Topside Model of Atmosphere and Ionosphere for Aeronomy (GAIA) is a global circulation model (GCM) giving neutral dynamics for all altitudes from the ground up to ~ 600 km (Jin et al., 2012). GAIA data has been compared and verified with experiment data from numerous different apparatuses for time spans up to several decades. The GAIA dataset used for the analysis presented in Section 5 has been previously applied for long term investigations in H. Liu et al. (2017) and Stober et al. (2021). We summarize the most important features and refer to these publications for more detailed information.

The atmosphere up to ~ 30 km altitude is constrained to the JRA-25/55 reanalysis (Onogi et al., 2007) using a nudging technique. While the solar irradiance is parametrized with the F10.7 index, the geomagnetic activity is set to a constant value. Therefore, the cross polar potential is held at 30 kV for all model data, corresponding to a moderate geomagnetic activity. The neutral wind components are provided on a grid with a resolution of 1° in latitude and 2.5° in longitude. The altitude resolution is 1/5 of the respective scale height at each altitude. The analysis presented in this paper has been conducted with preprocessed files giving the data in 10 km altitude bins. The time resolution is 0.5 h.

3.2 WACCM-X(SD)

The Community Earth System Model (CESM) is a combination of models covering different parts of the Earth system (Hurrell et al., 2013). The Whole Atmosphere Community Climate Model Extension WACCM-X (H.-L. Liu et al., 2018) is the part of the CESM describing the atmosphere from the ground up to $\gtrsim 500$ km. The data presented in this paper was generated with a *Special Dynamics* run WACCM-X(SD) (Gasperini et al., 2020) and previously used in Stober et al. (2021). Again, we only give a brief overview and refer to the mentioned publications.

The lower atmosphere is constrained up to ~ 50 km to NASA's reanalysis MERRA (Rienecker et al., 2011). Other than the used GAIA run, WACCM-X(SD) does not set a fixed cross polar potential. The polar convection is calculated using the *Heelis* model (Heelis et al., 1982) and the geomagnetic activity is therefore parametrized by the Kp index. The longitudinal resolution is 2.5° and values are given in 3h intervals. Since the model is evaluated on hydrostatic pressure levels, the altitude range extends from 992.5 hPa near the ground up to $\sim 4 \cdot 10^{-10}$ hPa. The height resolution above $\sim$ 50 km is 1/4 of the respective scale height. The corresponding geopotential altitudes are given for each time and position and range roughly from the ground up to ~ 500 km. In the transition region, the geopotential height resolution varies between 1 km and 5 km.

The different parametrization of geomagnetic activity in the used GAIA and WACCM-X runs are ideal to investigate its influence on neutral winds at different altitudes. However, since both models extend to the ground and are restrained to reanalysis of meteorological data (Stober et al., 2021), it is not feasible investigating the impact of atmospheric forcing in these models.

3.3 TIE-GCM

The Thermosphere Ionosphere Electrodynamic General Circulation Model (TIE-GCM) (Richmond et al., 1992) is a stand alone ionosphere model and also part of the Coupled Magnetosphere-Ionosphere-Thermosphere Model (CMIT) (Qian et al., 2014).

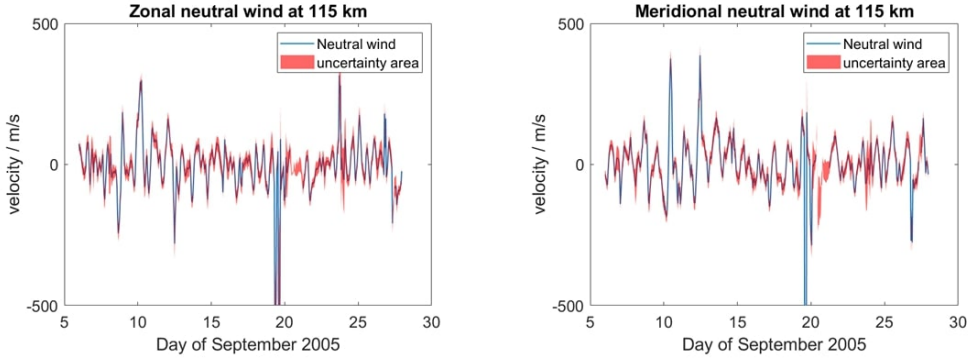

Figure 1. Neutral winds at 115 km altitude in zonal (left) and meridional (right) direction. The uncertainty has been determined from the measurement uncertainty by means of Gaussian error propagation.

The data presented in this paper was generated from several runs performed with the TIE-GCM Model Version 2.0.

In contrast to the two models described above, TIE-GCM does not extend down to the ground, but implies a lower boundary condition at ~ 99 km altitude. The horizontal neutral winds and neutral temperatures at the boundary are specified by input files. These quantities are calculated from the monthly averaged amplitudes and phases of diurnal and semidiurnal tides given by the Global Scale Wave Model (GSWM) (Hagan & Forbes, 2002, 2003). Performing separate runs with empirical GSWM tidal input, alternated values or no tidal input at all allows to assess the impact of atmospheric dynamics and the forcing from below. Same as for WACCM-X, the *Heelis* model is used to obtain the cross polar potentials and geomagnetic activity is parametrized according to the Heelis parametrization (Heelis et al., 1982). TIE-GCM gives output data on a 2.5° $\times$ 2.5° grid with a time resolution of 1h. Furthermore, TIE-GCM data is provided on logarithmic altitude coordinates (*atmospheric ln pressure coordinate*) $\ln\left(\frac{p_0}{p}\right)$ for the pressure p at a certain altitude. The reference pressure $p_0 = 5{\cdot}10^{-5}$ hPa corresponds roughly to ~ 225 km altitude and the atmospheric ln pressure coordinate ranges from -6.875 to 7.125 in 0.25 increments. This corresponds to a resolution of 1/4 in scale height units. The geopotential altitude ranges from ~ 96 km to ~ 590 km with a resolution that steadily increases from ~ 2 km to ~ 18 km with increasing height.

4 Experiment data

This section will give an overview on the results from analysis of experimental data with the instruments presented in Section 2. The most important features will be highlighted. Interpretation of these features and comparison to the results from model data analysis will be given in Section 6.

4.1 Neutral wind

As described in Section 2.1, three dimensional ion velocity vectors where calculated from four line of sight measurements and then used to derive three dimensional neutral wind vectors. Figure 1 shows the calculated neutral winds in zonal and meridional directions for the measurement channel corresponding to 115 km altitude.

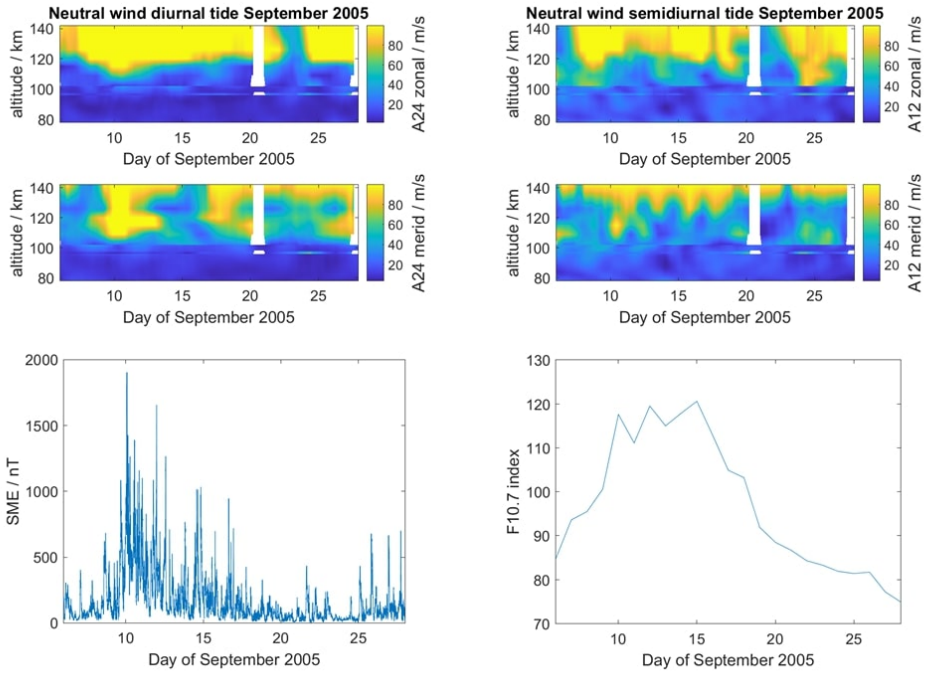

Figure 2. The upper row shows the amplitudes of diurnal (left) and semidiurnal (right) oscillations in zonal (top) and meridional (bottom) direction during September 2005. Data from EISCAT and meteor radar are merged together. The lower row shows the variations of geomagnetic activity (magnetic local time subset of the SME index, left) and the solar irradiation (F10.7 index, right) during the measurement time.

Error bars shown in Figure 1 are calculated from the ion velocity measurement uncertainties which affect the neutral wind values both directly and via the electric field calculation. Uncertainties of the ion-neutral collision frequency, which can have a major impact (Williams & Virdi, 1989), are not shown. While the relative uncertainties at altitudes $\gtrsim 110$ km are reasonably small ($\leq 40\%$), they tend to increase with decreasing altitudes ($\leq 70\%$). The lower electron density results in smaller signal-to-noise ratios and consequently to increased statistical uncertainties in the derived ISR parameters. Neutral wind velocities calculated from EISCAT measurements at low altitudes should therefore be treated carefully when looking at absolute values. The determination of tidal-like oscillation amplitudes, however, is still possible with reasonable accuracy compared to other altitudes since the ASF technique takes into account uncertainties of the input data. The strong outliers at single timepoints (around day 19) and data gaps (around day 21) visible in Figure 1, both likely caused by problems with the radar system, can also be handled by the ASF method.

The diurnal and semidiurnal amplitudes are determined separately for each altitude level. Figure 2 shows the amplitudes of tidal-like oscillations measured by the Kiruna meteor radar (80 km $\leq h \leq$ 104 km) and the EISCAT UHF in Tromsø (96 km $\leq h \leq$ 142 km). To see possible correlations, indices for geomagnetic activity and solar irradiation during the time of the measurement campaign are also shown in Figure 2. The SuperMAG Auroral Electrojet (SME) index and its subsets in magnetic local time (MLT) quantify the geomagnetic activity. A more detailed description will be given in Section 4.2. The F10.7 index is commonly used to quantify solar irradiation.

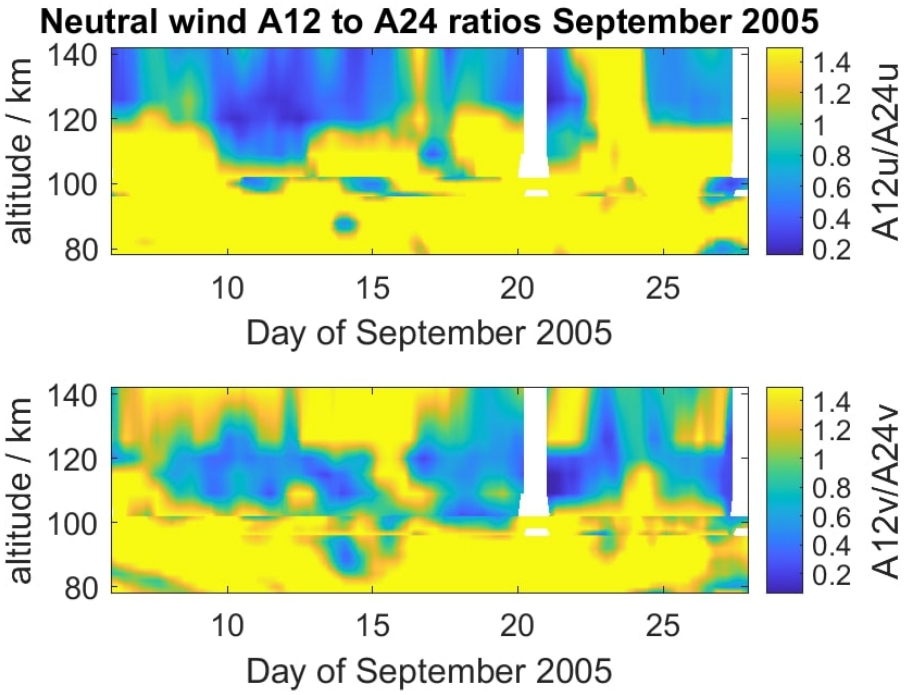

Figure 3. Ratio of semidiurnal to diurnal amplitudes shows two-band structure of dominant semidiurnal oscillations.

The figure shows the merged amplitudes of both systems and reflects the transition altitude between both instruments at about 100 km. Additionally, the graphic indicates the presence of a data gap around September 21st for the EISCAT observations, whereas the meteor radar wind time series remains uninterrupted during the entire period. Considering the different geographic locations of both instruments, which are about 100 km apart from each other, the similarity of the amplitudes in magnitude an variability is remarkable. Some features even seem to extend across the coverage gap (see A12 meridional, around September 15th). This strongly reinforces the validity of the neutral wind calculation method summarized in Section 2.1. Both oscillations show an increasing amplitude with altitude due to decreasing atmospheric density. Especially the diurnal oscillations are difficult to recognize at 120 km. The variability of diurnal and semidiurnal oscillations can now be compared and investigated concerning a different forcing mechanism.

The next step is the determination of the dominant tidal mode at each time and altitude. Therefore, the amplitude ratio of semidiurnal and diurnal oscillations is calculated and shown in Figure 3.

The ratio of zonal amplitudes A12u/A24u in the upper plot of Figure 3 corresponds very much to what is expected from the tidal theory (Lindzen, 1979). Semidiurnal variations are predominant up to altitudes of $\sim 110{-}120$ km. Above that, most of the time diurnal oscillations exhibit larger amplitudes. Meridional tidal amplitudes, however, indicate distinct differences and, thus, points out that this tidal component governed by additional more complicated physical processes. While the transition from predominant semidiurnal to diurnal tide also takes place at and around 110 km altitude, there is an upper band of strong semidiurnal oscillations especially during the first half of September. This apparent weakening of the upper SW2 band around equinox is an important feature since atmospherically forced SW2 tides have been shown to undergo such an au-

tumn transition (Pedatella et al., 2021). Whether this upper band is generated *in situ* or forced by some atmospheric tidal mode that propagates unusually far up remains to be investigated in more detail.

Assuming *in situ* generation being correlated to geomagnetic activity, one can apply a geomagnetic activity filter and thereby visualize how oscillations behave differently by setting thresholds to define high and low activity periods.

4.2 Geomagnetic activity filter

There are various indices quantifying the geomagnetic activity at different latitudes and sometimes also longitudes. At high latitudes, the Auroral Electrojet (AE) index is probably the most commonly used, measuring the strength of east- and westwards directed currents in the auroral zone. However, the AE index uses a set of stations spread across all longitudes. Since the measurements presented in this paper only cover a local region around $\sim$ 20° E longitude, it is more appropriate to use an index that also includes local subsets.

The SuperMAG Auroral Electrojet (SME) index (Newell & Gjerloev, 2011) is calculated from magnetometer data taken by all stations of the SuperMAG network in a latitudinal range from 40° N to 80° N. Additionally to a global index value, the SME index is given in 24 local sub-channels, each covering one hour of magnetic local time (MLT) (Newell & Gjerloev, 2014). Knowing the magnetic local time at Tromsø (MLT = UTC + 2.5), it is possible to bin the data time intervals corresponding to the appropriate MLT channel for each observation and, thereby, generating a local SME index.

A superposed epoch analysis (SEA) (Singh & Badruddin, 2006) is performed on a set of local SME indices for each of the 30 days during September 2005. To filter out high activity periods, a local SME index filter threshold $0.0 \leq T_{SME} \leq 1.0$ is defined. For instance $T_{SME} = 0.9$ means that for each time of day, the ten percent highest activity observations are not included in the analysis. Figure 4 shows the diurnal and semidiurnal amplitudes in the meridional neutral wind determined for three different datasets with different T_{SME} values.

It should be noted here again, that while the amplitudes are fitted on the data with a temporal resolution of 6 min, the amplitudes are averaged using a one day sliding window. Therefore, gaps in the presented data will only occur if the SME index is consistently above the defined threshold for at least a full day. Shorter high activity periods will not be considered for the ASF fitting, but an amplitude value is given for these times due to the averaging. The possibility of ASF being applied on a dataset with notable gaps is central at this point.

The upper row of Figure 4 shows the unfiltered ($T_{SME} = 1.0$) meridional amplitudes. Both amplitudes maximise for higher altitudes. There are periods, most notably at and shortly after day 10, where large diurnal amplitudes seem to be present at lower altitudes. A similar effect, but weaker, is observed for semidiurnal amplitudes at the same time. The analysis on the filtered datasets for $T_{SME} = 0.9$ and $T_{SME} = 0.8$ indicates that such enhancements of the diurnal amplitudes at lower altitudes appears to be connected to periods of consistently high geomagnetic activity. Shorter time intervals of high activity exhibit a much weaker effect since the amplitudes of the filtered data changes only slightly compared to the unfiltered observations during the rest of the month. The increase of diurnal amplitude for stronger geomagnetic activity could be expected since the convection electric fields are directly connected to auroral currents. The fact that a similar correlation is observed for the semidiurnal tidal amplitudes suggests, however, that this tidal mode also depends on the geomagnetic activity. This would mean that semidiurnal oscillations at high altitudes are not the result of upwards propagating atmospheric tides. The upper altitude band seen in Figure 3 would rather be *in situ* generated according to this.

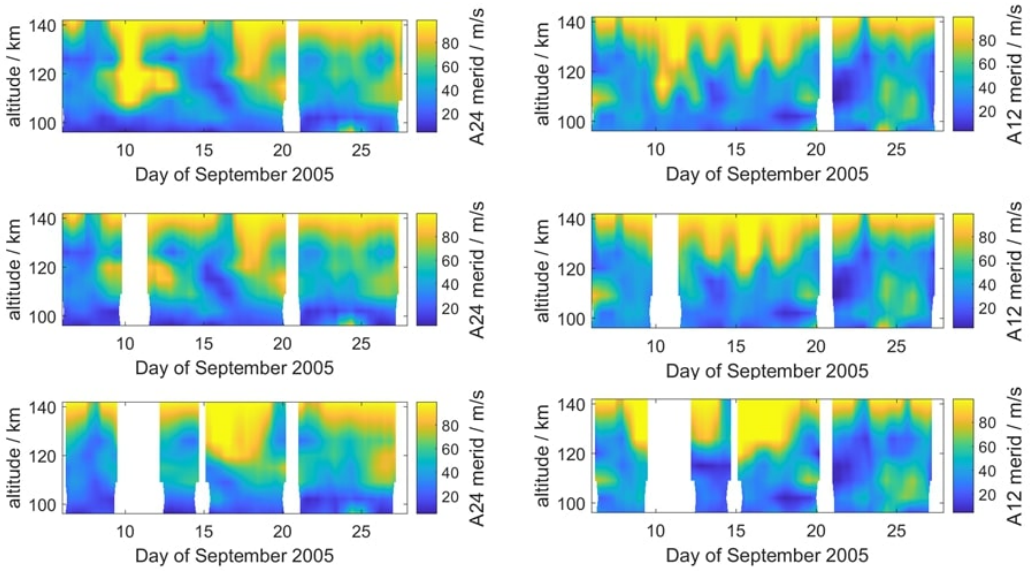

Figure 4. Geomagnetic impact on meridional amplitudes of diurnal (left) and semidiurnal (right) oscillations shown by comparison of amplitudes with local SME index thresholds $T_{SME} = [1.0; 0.9; 0.8]$ (from the top). For both diurnal and semidiurnal oscillations, strong amplitudes reaching down to 120 km can be associated with high geomagnetic activity.

If the semidiurnal variations are indeed connected to the same convection electric fields as the diurnal oscillations, the 12h amplitude should be visible in the ion velocities at higher altitudes as well.

4.3 High altitude ion velocities

F-region neutral winds are inferred from the ion velocity observations of EISCAT. The ion velocities at ~ 300 km altitude permit to estimate the convection electric field required in Equation 1. Furthermore, these high altitude ion velocities can now be directly investigated for periodicities. Diurnal and semidiurnal amplitudes are shown in Figure 5.

The diurnal amplitudes exhibit a pronounced peak at and shortly after day 10, which occurs coincidentally with the increased geomagnetic activity. A second, smaller peak, at day 15 can also be attributed to geomagnetic activity. At the magnetic latitude MLAT 67 in Tromsø, the stronger zonal variations fit the two cell convection pattern very well, whereas closer to the geomagnetic pole the meridional component becomes dominant (Wu et al., 2017). The semidiurnal oscillations exhibit a very similar pattern with distinct peaks during high activity periods. Furthermore, the diurnal and semidiurnal wind variations are stronger in the zonal component than in the meridional. As expected, the semidiurnal amplitudes are weaker compared to the diurnal amplitudes. However, the 12h variations shown in Figure 5 are notably higher than a higher harmonic of 24h oscillation. This leads to the conclusion that polar convection might force semidiurnal oscillations. Possible reasons for this are discussed in Section 6.

To obtain more information about the spatial shape of this semidiurnal tidal-like oscillations and its origin, global model data is analysed.

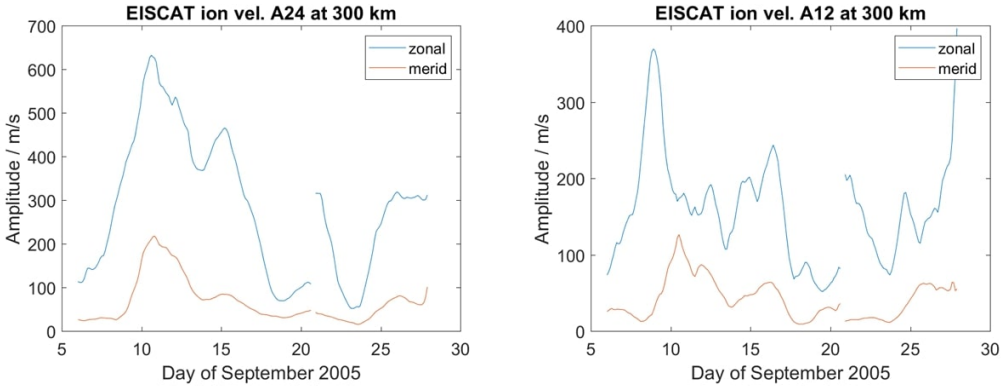

Figure 5. Diurnal (left) and semidiurnal (right) amplitudes in the ion velocities from the F-region altitude channel measured with EISCAT.

5 Model data

This section will give an overview on the results from analysis of global simulation data with the models presented in Section 3. The most important features will be highlighted. Interpretation of these features and comparison to the results from measurement data analysis will be given in Section 6.

5.1 Neutral wind

GCM models provide neutral wind velocities on a global longitude and latitude grid. The data is analyzed in the range from day 200 to 320 (July 19th to November 16th) of the year 2005. The plots in this Section are restricted to the days of the EISCAT measurement campaign to allow a direct comparison of the dynamics over these days. The neutral wind velocities are analysed at a single latitude corresponding to Tromsø for all datasets. Furthermore, the GCM longitudinal resolution is the same in all models with 2.5°.

As described in Section 1, the ASF here fits not only for the time period of neutral wind oscillations but also for zonal wave numbers $0 \leq k \leq 3$. To compare the model data with the measurements, the perspective of a local observer needs to be taken into account. The resultant amplitudes of the combined migrating and non-migrating modes were extracted at 20° E longitude to ensure that a comparison with the observations is meaningful. As expected, the clearly dominating tidal-like modes for both diurnal and semidiurnal oscillations are the sun-synchronous modes DW1 and SW2. Therefore, we only present the obtained amplitudes for these modes.

To investigate the impact of different forcings from below, model runs with different lower boundaries are compared.

5.1.1 Impact of geomagnetic activity (GAIA and WACCM-X(SD))

As described in Section 3, the GAIA applies a constant cross polar potential corresponding to a low geomagnetic activity. The impact of geomagnetic activity will be determined by comparison to the WACCM-X(SD) run. However, since polar convection is not completely switched off in the GAIA, the impact of the convection pattern can only be determined by comparing data from both models and data from the mid-latitudes, which should be almost not affected by the geomagnetic activity.

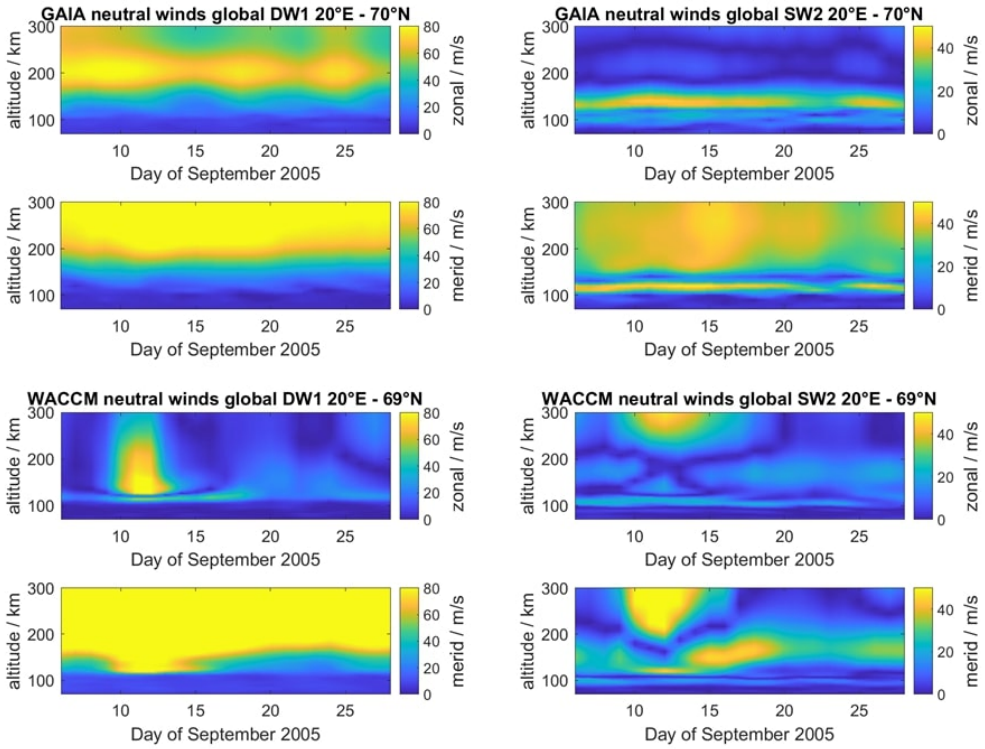

Figure 6. Comparison of GAIA (top) and WACCM-X(SD) (bottom) amplitudes of the DW1 (left) and SW2 (right) tidal modes at high latitudes (70° N).

Figure 6 shows the amplitudes of DW1 and SW2 obtained from GAIA and WACCM-X(SD) data evaluated at the Tromsø geographical position.

To ensure comparability between data from model runs with different forcing or evaluated at different latitudes, the colour scale is kept the same for all view graphs. Within the expected deviations due to different handling of geomagnetic activity, the models show similar tidal-like behaviour:

The diurnal oscillations exhibit large amplitudes in the meridional component at high altitudes in both models during the selected time interval. This indicates that oscillations forced by plasma convection in the F-region have a larger impact on the transition region processes for higher geomagnetic activity.

The semidiurnal amplitudes indicate a pronounced maximum band at or slightly above ~ 100 km altitude in both models and for the zonal and meridional direction. According to classical tidal theory, this is associated with upward propagating atmospheric tides. The amplitude of vertically propagating tides is supposed to show an exponential growth with increasing altitude. However, at the lower transition region the wave energy starts to be dissipated due to the ion drag (Smith, 2012). Additionally, both simulations show a multi-band structure of strong semidiurnal amplitudes. GAIA shows two bands in both zonal and meridional direction with the upper band extending down to $\sim 130 - 160$ km. This upper band is clearly more influential in meridional direction, linking it to the convection pattern, and seems to undergo a transition process around the autumn equinox. This autumn transition can also be found in the WACCM-X(SD) data. This run even exhibits a third band at altitudes $\gtrsim 200$ km. Here, we will focus on the second band which is taken to correspond to the upper band in the GAIA run. This second band reflects strong semidiurnal oscillations, which appear to be inhibited

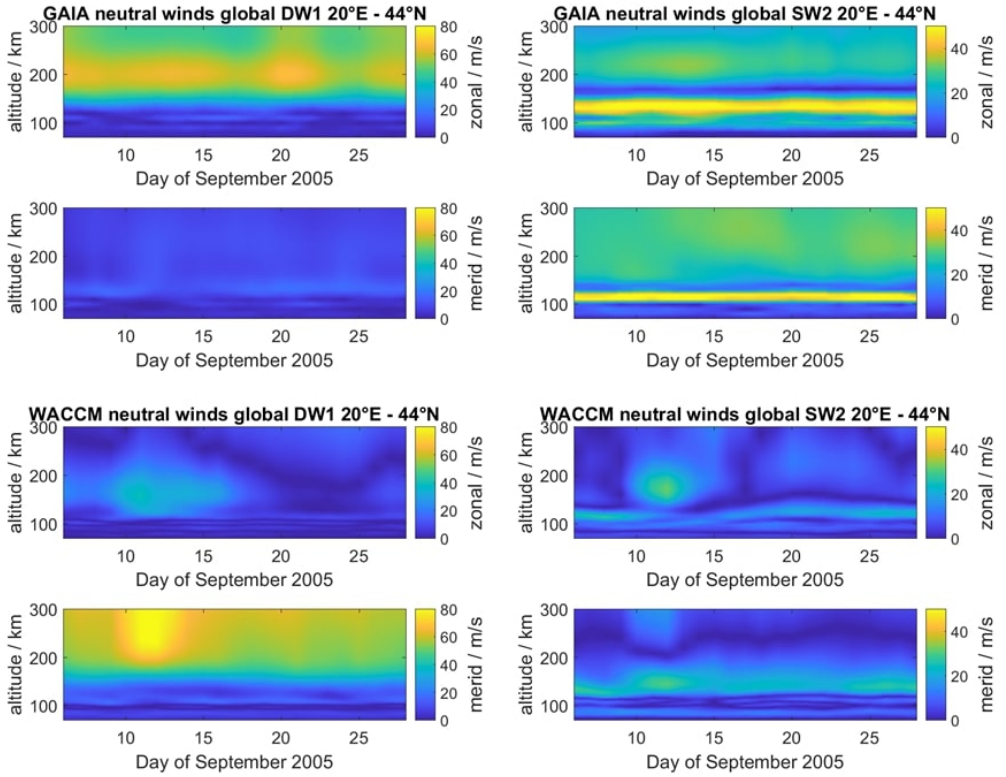

Figure 7. Comparison of GAIA (top) and WACCM-X(SD) (bottom) amplitudes of the DW1 (left) and SW2 (right) tidal modes at mid latitudes (44° N).

or not excited in zonal direction, presumably also due to the larger extension of the convection pattern as discussed before.

In conclusion, it can be said that both model runs agree in various important and unexpected features, mostly the multi-band structure of the SW2 tidal-like mode. Though there are distinct differences, these seem to be mostly caused by the different parametrization of geomagnetic activity. A forcing of both DW1 and SW2 oscillations by polar plasma convection seem to provide a reasonable explanation of the observed results.

To investigate this conclusion even further, one can look at the neutral wind data from the same model runs at mid-latitudes where the polar convection should have no influence. Figure 7 shows the exact same tidal-like modes as Figure 6 but at 44° northern latitude.

The diurnal amplitudes are decreased in both models for both directions at all altitudes. This monotonous decrease strongly indicates polar convection to be a major source of neutral wind oscillations. It can also be seen that the decrease is stronger in meridional direction where the amplitudes went down to almost negligible magnitude in GAIA and significantly reduced compared to the strong amplitudes in WACCM-X(SD). While also smaller, the zonal amplitudes underwent less of a reduction going from high- to mid-latitudes. The meridional DW1 oscillations are definitely connected to high latitude effects. For zonal oscillations there seems to be at least one other significant effect which has nearly equal strength at polar and mid-latitudes.

The SW2 oscillation maximum at ~ 100 km associated with upward propagating tides is also visible at lower latitudes, providing confidence to our previous interpretation. The upper band is missing in the WACCM-X(SD) data. This is contrary to GAIA,

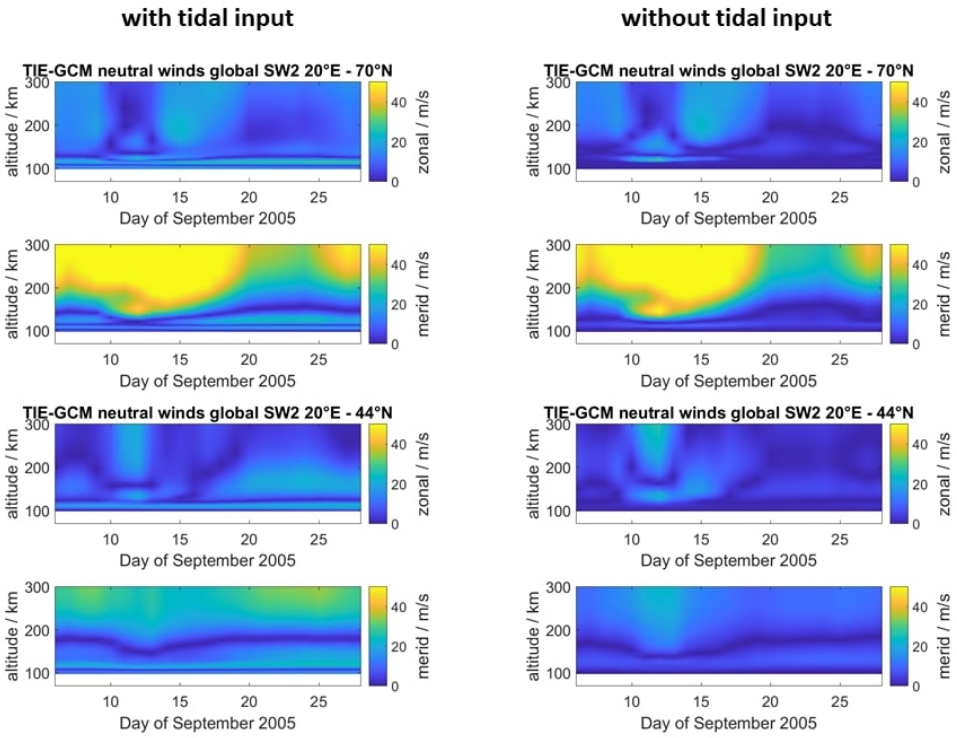

Figure 8. Amplitudes of SW2 tidal-like oscillation from the TIE-GCM model at high (up) and mid-latitudes (bottom). Presented are two separate runs with realistic (left) and zero (right) atmospheric tidal input.

which indicates an upper band of strong semidiurnal oscillations. The transition of the SW2 oscillations observed around autumn equinox seems to be reversed at mid-latitudes with the upper band tending to gain intensity afterwards. This transition and the fact that the upper SW2 band does not completely vanish at mid-latitudes indicates that it might not be forced only by polar plasma convection but rather due to an interplay of several processes. Different wave modes forced by these processes interfere. If the forcing changes, this can lead to a change from constructive to destructive interference. Different interference of the wave modes could explain the sudden transitions observed around equinox.

5.1.2 Impact of atmospheric forcing (TIE-GCM)

Comprehensive models such as GAIA and WACCM-X involve complex processes, which have to be parametrized posing challenges to conduct and investigate more isolated processes. TIE-GCM offers the possibility to investigate the ionosphere and thermosphere by applying a well-defined lower boundary condition describing the middle atmospheric forcing. Figure 8 shows the results of two different model runs, one performed using an empirical input for tidal oscillations at 99 km and one with tidal amplitudes set to zero at the boundary. The dominance of sun-synchronous tidal-like modes and the behaviour of DW1 oscillations are similar as found in other models. Therefore, further investigations are restricted to SW2 oscillations from these model runs.

Additionally to different atmospheric boundary conditions, different latitudes are considered as well. At high latitudes, the TIE-GCM run with empirical GSWM tidal forc-

ing exhibits a SW2 amplitude structure that resembles the tidal fields very similar to the ones shown in Figure 6 from GAIA and WACCM-X(SD). This run indicates a two band structure accompanied by a transition of the upper band around the autumn equinox. Though, the lower band is notably weaker than in the other models suggesting that the tidal amplitudes are underestimated for the lower boundary. This is confirmed when comparing the amplitudes of TIE-GCM initialized with a zero tidal activity at the lower boundary. In this model run, the lower band mostly vanishes, whereas the upper band appears to be not affected, which also excludes an atmospheric forcing as origin of the upper SW2 band structure. It should be noted, that propagating tides forced by EUV absorption above the lower boundary are still present in TIE-GCM. At mid-latitude, we obtain a similar picture as already found in Figure 7, showing a notably reduced SW2 amplitude at high altitudes and a nearly unaffected amplitude at lower altitudes. Most interestingly here, even the high altitude SW2 oscillations are still visible and seem to be forced by the propagating tides from the middle atmosphere, since they vanish in the run with artificially zero tidal forcing at the lower boundary. Prompting the same conclusion of the upper SW2 band being linked to the polar plasma convection, this also brings new insight regarding the transition around equinox. Indeed, there seem to be several processes that drive SW2-like oscillations and the observed autumn transition seems to be caused by their interaction.

5.2 Phase progression analysis

Phase progression analysis permits to distinguish between propagating tidal modes and *in situ* generated evanescent modes. The time of maximum should be steadily shifted with altitude for an upwards propagating oscillation, showing as a swift change of phase. Semidiurnal oscillations observed in EISCAT data below 120 km have been identified to correspond to upward propagating atmospheric tides (Nozawa et al., 2010). Furthermore, the model data is used in this paper to extend the altitude coverage well into the F-layer at mid- and polar-latitudes. Figure 9 shows the time of maximum of the semidiurnal oscillations in the meridional winds extracted from GAIA and WACCM-X(SD). To emphasize the autumn transition seen in the oscillation amplitudes, the whole range of model data from day 200 to day 320 is shown here.

Both models show a steady phase progression at low altitudes and nearly constant phase at higher altitudes. The boundary between progressing and constant phase is notably higher up in GAIA which is related to the fixed low geomagnetic activity in the model. For both models, the boundaries are found at similar altitudes as the upper SW2 band in Figure 6. This clearly reinforces the conclusion that the lower SW2 band is caused by upwards propagating atmospheric tides and the upper SW2 band is *in situ* forced. The mentioned boundary between progressing and constant phase additionally allows to mark the transition from dominant solar to terrestrial atmospheric dynamical forcing. The sudden transition around equinox (DOY 265) is also visible in the phases, especially from GAIA data at high latitudes. This suggests a strongly increased propagation of atmospheric tides as main cause for the transition. WACCM-X(SD) uses much stronger geomagnetic activity which counteracts the upwards propagation of tides. This might explain why the transition is more pronounced in GAIA data. At mid-latitudes, both models show a steady change of the phase boundary. The reversed transition of the upper SW2 band seen in Figure 7 cannot be explained from the shown phase progression. However, phase progression analysis is a helpful technique to quantify the respective influence of geomagnetic and atmospheric forces and to identify the altitude where the dominant processes change.

5.3 High altitude ion velocities

Since the high altitude ion velocity oscillations are measured in EISCAT at 300 km altitude, the reliability of the model data at high altitudes can be partially verified. Con-

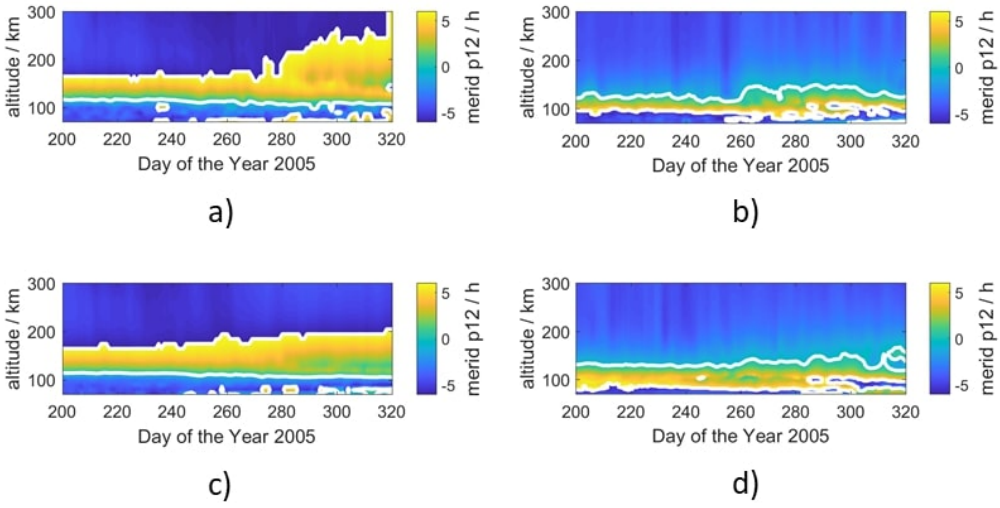

Figure 9. Phase progression of the SW2 mode from GAIA (a and c) and WACCM-X(SD) (b and d) at high latitudes (a and b) and mid-latitudes (c and d). Both models give a nearly constant phase at the altitudes of the upper band, indicating an *in situ* generation of this band.

sidering that GAIA uses a constant cross-polar potential, it is expected that plasma convection ion velocities should indicate increased discrepancies compared to the ISR observations. WACCM-X(SD) and TIE-GCM include the Kp index to parametrize geomagnetic activity and therefore should achieve a better agreement in the ion velocities resembling the measurements. Figure 10 shows diurnal and semidiurnal oscillation amplitudes of the ion velocity at 300 km altitude from GAIA, WACCM-X(SD) and TIE-GCM.

It can be seen that the diurnal oscillation amplitudes are dominant and indicate reasonable agreement for TIE-GCM and WACCM-X(SD), which was already found for the geomagnetic activity. Semidiurnal oscillations also have significant amplitudes and tentatively also correspond to the geomagnetic activity. It can be concluded that semidiurnal oscillations at high altitudes are forced by the same plasma convection as diurnal oscillations. GAIA ion velocity amplitudes are similar to WACCM-X(SD) and TIE-GCM amplitudes at low activity times and show little variability. The ion velocity oscillations of WACCM-X(SD) and TIE-GCM are highly similar in amplitudes and dynamics.

6 Interpretation of results from measurements and models

The first part of this study evaluated the validity of both EISCAT measurements in comparison to the model fields from GAIA and WACCM-X(SD). The neutral wind computation method applied to EISCAT data was verified with meteor radar measurements for the overlapping altitude region. From the combined data set, combined neutral wind measurements from $\sim 80-140$ km altitude were derived. Since meteor radars have proven to be a highly reliable and worldwide used technique (see Section 2.2 and references there within), the good agreement between EISCAT and meteor radar amplitudes suggests a good reliability of both neutral wind data products. The most important feature found from the analysis of the EISCAT measurements was an upper band of unexpectedly strong semidiurnal oscillations. Comparison with the results from three separate ionosphere GCM models confirmed a two band structure of 12h modulations

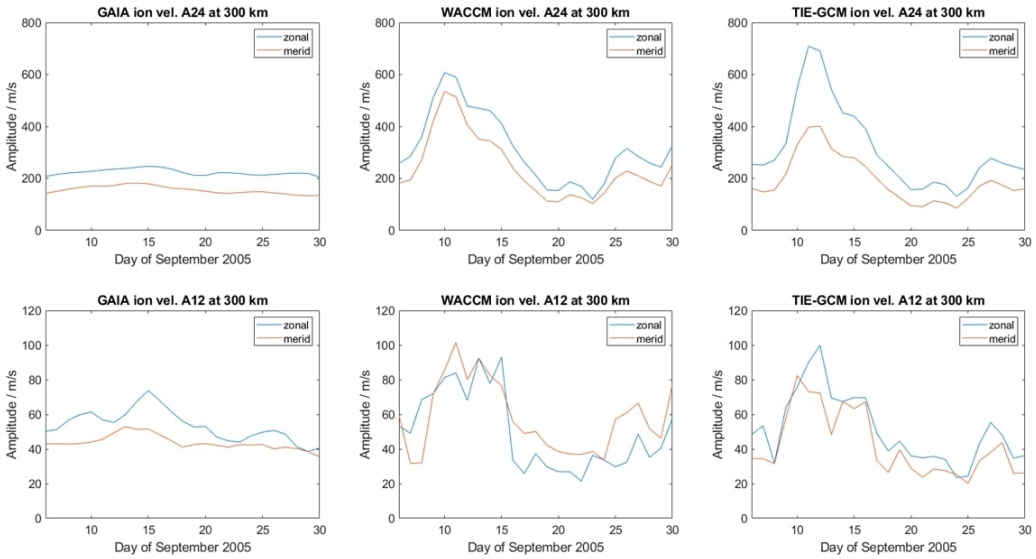

Figure 10. Diurnal (top) and semidiurnal (bottom) high altitude ion velocity amplitudes from GAIA, WACCM-X(SD) and TIE-GCM (left to right).

in the ionosphere. However, the three models all give different amplitudes and indicate altitudinal differences of the transition regions between the 12h oscillation bands. We attribute this to different handling of geomagnetic activity and the cross-polar potential, which affects the plasma convection pattern and strength within the polar cap. The observed lowest altitude of the upper semidiurnal oscillation band of $\sim$ 120 km $-$140 km is well within the possible range given by WACCM-X(SD) and TIE-GCM. These use a more realistic approximation of geomagnetic activity than the GAIA. The application of a geomagnetic activity filter on the EISCAT data revealed that at high altitudes both diurnal and semidiurnal oscillations are forced by geomagnetic activity. For high activity, strong oscillation amplitudes can reach down to low altitudes. This is supported by large amplitudes even down to low altitudes in those models which do not assume a generally low geomagnetic activity. The comparison with mid-latitudes also in global models further reinforces the measurement finding by suggesting the polar plasma convection as origin of the upper semidiurnal oscillation band found with EISCAT. Additional to the apparent linkage to geomagnetic activity, the upper semidiurnal band seems to be nearly independent from atmospheric forcing. Two TIE-GCM runs with and without atmospheric boundary at $\sim$ 99 km show that while the lower 12h band vanishes when a net zero tidal atmospheric forcing is applied, however, the upper semidiurnal oscillation region remains unchanged. This renders atmospheric forcing of the observed two band structure unlikely. However, the transition of the upper SW2 band around equinox as seen in all three models as well as EISCAT (also previously reported by Nozawa et al. (2010)) is very similar to what is expected for the lower SW2 band (Pedatella et al., 2021). In fact, the GAIA and WACCM-X(SD) runs clearly show transitions of the lower SW2 band at similar times as the upper one. This underlines a potential *in situ* forcing of high altitude SW2 oscillations, a possible connection to atmospheric dynamics remains with the observed autumn transition. The conclusion of forcing from above and below each being responsible for one of the observed regions is confirmed by the phase progression analysis. The phases of semidiurnal oscillations in the investigated model runs show a transition from phase propagation at low altitudes, corresponding to vertically propagating tidal modes, and a constant phase at high altitudes suggesting an in situ generation. Phase progression analysis also reveals a defined altitude at which the dom-

inant impact changes from atmospheric to geomagnetic forcing, marking a very important point for ionospheric dynamic. Again, different models show diverse transition altitudes due to different implementations of the geomagnetic activity. Furthermore, we report another feature that was found by comparing high altitude ion velocities from EISCAT, WACCM-X(SD) and TIE-GCM, which reflect in the general morphology and also the amplitudes. However, the relative amplitudes between zonal and meridional ion velocities reflect distinct differences, which are not entirely understood. This might be connected with different shapes and sizes of the polar convection pattern and consequently different positioning of the evaluated grid point within this pattern. GAIA and WACCM-X(SD) apply different approaches on how the geomagnetic activity is implemented in the models resulting in different plasma convection patterns. In addition, the deviation of the *Heelis* model from the actual polar convection is not yet fully understood and requires further investigations that are beyond the present paper.

7 Conclusion

It has been shown that it is possible to perform continuous and combined observations of neutral wind velocities with meteor radars and incoherent scatter radars. Such simultaneous observations are of major importance when studying the coupling of atmospheric phenomena into the ionosphere. Another methodological improvement in this paper is the first use of the ASF technique on EISCAT measurements. This technique permits to resolve the day-to-day variability of unevenly sampled time series and an improved handling of the measurement uncertainties which are highly relevant in the ISR method. The thereby enabled larger altitude range revealed a previously not reported two band structure of strong semidiurnal oscillations. Using several global ionosphere models, we confirmed the measured two band structure and showed that both diurnal and semidiurnal tidal-like oscillations are sun-synchronous (DW1 and SW2). Phase progression analysis and different atmospheric boundaries settings showed that the lower SW2 band is presumably a upwards propagating atmospheric tide. Tidal-like oscillations higher up are *in situ* forced and related to geomagnetic activity as shown in measurements. Comparing models at high and mid-latitudes suggest the origin of this forcing to be the polar plasma convection. The autumn transition of the high altitude SW2 oscillation, seen both in measurements and model, resembles a previously reported autumn transition of SW2 oscillations (Pedatella et al., 2021). This suggests the existence of more than one forcing process. The exact mechanism behind this remains to be identified and studied in future investigations. The same goes for the suspected differences of size and shape of the plasma convection pattern in different models and reality which might be responsible for discrepancies in the relation of zonal and meridional dynamics.

Open Research

The model and measurement data used in this paper as well as the input files for the conducted TIE-GCM runs can be found under doi:10.5281/zenodo.6343418 (Günzkofer et al., 2022). In case of further questions about the data and the used analysis software please contact the corresponding author. The analysis software will be shared upon request.

Acknowledgments

The authors would like to acknowledge the following data sources:
EISCAT is an international association supported by research organisations in China (CRIRP), Finland (SA), Japan (NIPR and ISEE), Norway (NFR), Sweden (VR), and the United Kingdom (UKRI).
We gratefully acknowledge the SuperMAG collaborators (http://supermag.jhuapl.edu/info/?page=acknowledgement) for providing the SME index.

For this study, a dataset from the Ground-to-topside model of Atmosphere and Ionosphere for Aeronomy (GAIA) project carried out by the National Institute of Information and Communications Technology (NICT), Kyushu University, and Seikei University was used.
The WACCM-X model has been developed at NCAR (see https://www2.hao.ucar.edu/modeling/waccm-x).
The TIEGCM and related Thermosphere-Ionosphere models have been developed by the "Atmosphere Ionosphere Magnetosphere" (AIM) Section of the High Altitude Observatory (HAO) at NCAR (see http://www.hao.ucar.edu/modeling/tgcm). The TIEGCM data was generated on the 'Kratos' High-Performance Data Analysis Cluster (HPDA).

References

Andrews, D. G., Holton, J. R., & Leovy, C. B. (1987). *Middle atmosphere dynamics.*

Barraclough, D. R. (1988, April). IAGA Division I Working Group 1: International Geomagnetic Reference Field revision 1987. *Geophysical Journal International*, *93*(1), 187-189. doi: 10.1111/j.1365-246X.1988.tb01397.x

Baumgarten, K., & Stober, G. (2019). On the evaluation of the phase relation between temperature and wind tides based on ground-based measurements and reanalysis data in the middle atmosphere. *Annales Geophysicae*, *37*(4), 581–602. Retrieved from `https://angeo.copernicus.org/articles/37/581/2019/` doi: 10.5194/angeo-37-581-2019

Brekke, A., Doupnik, J. R., & Banks, P. M. (1973, December). A preliminary study of the neutral wind in the auroral E region. , *78*(34), 8235-8250. doi: 10.1029/JA078i034p08235

Chapman, S. (1956, August). The electrical conductivity of the ionosphere: A review. *Il Nuovo Cimento*, *4*(S4), 1385-1412. doi: 10.1007/BF02746310

Collis, P. N. (1995, August). EISCAT data base for ionospheric modelling: F-region and topside ionosphere. *Advances in Space Research*, *16*(1), 37-46. doi: 10.1016/0273-1177(95)00096-W

Folkestad, K., Hagfors, T., & Westerlund, S. (1983, December). EISCAT: An updated description of technical characteristics and operational capabilities. *Radio Science*, *18*(6), 867-879. doi: 10.1029/RS018i006p00867

Gasperini, F., Liu, H., & McInerney, J. (2020, May). Preliminary Evidence of Madden-Julian Oscillation Effects on Ultrafast Tropical Waves in the Thermosphere. *Journal of Geophysical Research (Space Physics)*, *125*(5), e27649. doi: 10.1029/2019JA027649

Grassmann, V. (1993, April). An incoherent scatter experiment for the measurement of particle collisions. *Journal of Atmospheric and Terrestrial Physics*, *55*(4-5), 573-576. doi: 10.1016/0021-9169(93)90006-K

Günzkofer, F., Pokhotelov, D., Stober, G., Liu, H., Liu, H., Mitchell, N. J., ... Borries, C. (2022, March). *Determining the origin of tidal oscillations in the ionospheric transition region with EISCAT radar and global simulation data.* Zenodo. ([Dataset]) doi: 10.5281/zenodo.6343418

Hagan, M. E., & Forbes, J. M. (2002, December). Migrating and nonmigrating diurnal tides in the middle and upper atmosphere excited by tropospheric latent heat release. *Journal of Geophysical Research (Atmospheres)*, *107*(D24), 4754. doi: 10.1029/2001JD001236

Hagan, M. E., & Forbes, J. M. (2003, February). Migrating and nonmigrating semidiurnal tides in the upper atmosphere excited by tropospheric latent heat release. *Journal of Geophysical Research (Space Physics)*, *108*(A2), 1062. doi: 10.1029/2002JA009466

Hedin, A. E. (1991, February). Extension of the MSIS thermosphere model into the middle and lower atmosphere. , *96*(A2), 1159-1172. doi: 10.1029/90JA02125

Heelis, R. A., Lowell, J. K., & Spiro, R. W. (1982, August). A model of the

high-latitude ionospheric convection pattern. , *87*(A8), 6339-6345. doi: 10.1029/JA087iA08p06339

Hocking, W. K., Fuller, B., & Vandepeer, B. (2001, January). Real-time determination of meteor-related parameters utilizing modern digital technology. *Journal of Atmospheric and Solar-Terrestrial Physics*, *63*(2-3), 155-169. doi: 10.1016/S1364-6826(00)00138-3

Hurrell, J. W., Holland, M. M., Gent, P. R., Ghan, S., Kay, J. E., Kushner, P. J., ... Marshall, S. (2013, September). The Community Earth System Model: A Framework for Collaborative Research. *Bulletin of the American Meteorological Society*, *94*(9), 1339-1360. doi: 10.1175/BAMS-D-12-00121.1

Jin, H., Miyoshi, Y., Pancheva, D., Mukhtarov, P., Fujiwara, H., & Shinagawa, H. (2012, October). Response of migrating tides to the stratospheric sudden warming in 2009 and their effects on the ionosphere studied by a whole atmosphere-ionosphere model GAIA with COSMIC and TIMED/SABER observations. *Journal of Geophysical Research (Space Physics)*, *117*(A10), A10323. doi: 10.1029/2012JA017650

Kelly, M. C. (2009). *The Earth's Ionosphere: Plasma Physics and Electrodynamics, Second Edition*.

Lee, W., Kim, Y. H., Lee, C., & Wu, Q. (2018, December). First Comparison of Mesospheric Winds Measured with a Fabry-Perot Interferometer and Meteor Radar at the King Sejong Station (62.2°S, 58.8°W). *Journal of Astronomy and Space Sciences*, *35*, 235-242. doi: 10.5140/JASS.2018.35.4.235

Lindzen, R. S. (1979, January). Atmospheric Tides. *Annual Review of Earth and Planetary Sciences*, *7*, 199. doi: 10.1146/annurev.ea.07.050179.001215

Liu, H., Sun, Y.-Y., Miyoshi, Y., & Jin, H. (2017, May). ENSO effects on MLT diurnal tides: A 21 year reanalysis data-driven GAIA model simulation. *Journal of Geophysical Research (Space Physics)*, *122*(5), 5539-5549. doi: 10.1002/2017JA024011

Liu, H.-L., Bardeen, C. G., Foster, B. T., Lauritzen, P., Liu, J., Lu, G., ... Wang, W. (2018, February). Development and Validation of the Whole Atmosphere Community Climate Model With Thermosphere and Ionosphere Extension (WACCM-X 2.0). *Journal of Advances in Modeling Earth Systems*, *10*(2), 381-402. doi: 10.1002/2017MS001232

Newell, P. T., & Gjerloev, J. W. (2011, December). Evaluation of SuperMAG auroral electrojet indices as indicators of substorms and auroral power. *Journal of Geophysical Research (Space Physics)*, *116*(A12), A12211. doi: 10.1029/2011JA016779

Newell, P. T., & Gjerloev, J. W. (2014, December). Local geomagnetic indices and the prediction of auroral power. *Journal of Geophysical Research (Space Physics)*, *119*(12), 9790-9803. doi: 10.1002/2014JA020524

Nicolls, M. J., Bahcivan, H., Häggström, I., & Rietveld, M. (2014, December). Direct measurement of lower thermospheric neutral density using multifrequency incoherent scattering. , *41*(23), 8147-8154. doi: 10.1002/2014GL062204

Nozawa, S., & Brekke, A. (1999, January). Studies of the auroral E region neutral wind through a solar cycle: Quiet days. , *104*(A1), 45-66. doi: 10.1029/1998JA900013

Nozawa, S., Ogawa, Y., Oyama, S., Fujiwara, H., Tsuda, T., Brekke, A., ... Fujii, R. (2010, August). Tidal waves in the polar lower thermosphere observed using the EISCAT long run data set obtained in September 2005. *Journal of Geophysical Research (Space Physics)*, *115*(A8), A08312. doi: 10.1029/2009JA015237

Oberheide, J., Forbes, J. M., Zhang, X., & Bruinsma, S. L. (2011, November). Climatology of upward propagating diurnal and semidiurnal tides in the thermosphere. *Journal of Geophysical Research (Space Physics)*, *116*(A11), A11306. doi: 10.1029/2011JA016784

Onogi, K., Tsutsui, J., Koide, H., Sakamoto, M., Kobayashi, S., Hatsushika, H., ... Taira, R. (2007, January). The JRA-25 Reanalysis. *Journal of the Meteorological Society of Japan*, *85*(3), 369-432. doi: 10.2151/jmsj.85.369

Pedatella, N. M., Liu, H. L., Conte, J. F., Chau, J. L., Hall, C., Jacobi, C., ... Tsutsumi, M. (2021, February). Migrating Semidiurnal Tide During the September Equinox Transition in the Northern Hemisphere. *Journal of Geophysical Research (Atmospheres)*, *126*(3), e33822. doi: 10.1029/2020JD033822

Picone, J. M., Hedin, A. E., Drob, D. P., & Aikin, A. C. (2002, December). NRLMSISE-00 empirical model of the atmosphere: Statistical comparisons and scientific issues. *Journal of Geophysical Research (Space Physics)*, *107*(A12), 1468. doi: 10.1029/2002JA009430

Pokhotelov, D., Becker, E., Stober, G., & Chau, J. L. (2018, June). Seasonal variability of atmospheric tides in the mesosphere and lower thermosphere: meteor radar data and simulations. *Annales Geophysicae*, *36*(3), 825-830. doi: 10.5194/angeo-36-825-2018

Qian, L., Burns, A. G., Emery, B. A., Foster, B., Lu, G., Maute, A., ... Wang, W. (2014). The ncar tie-gcm: A community model of the coupled thermosphere/ionosphere system, in *Modeling the Ionosphere-Thermosphere System*, geophysical monograph series, vol. 201. In (p. 73-83). American Geophysical Union. doi: 10.1002/9781118704417.ch7

Richmond, A. D., Ridley, E. C., & Roble, R. G. (1992, March). A thermosphere/ionosphere general circulation model with coupled electrodynamics. , *19*(6), 601-604. doi: 10.1029/92GL00401

Rienecker, M. M., Suarez, M. J., Gelaro, R., Todling, R., Bacmeister, J., Liu, E., ... Woollen, J. (2011, July). MERRA: NASA's Modern-Era Retrospective Analysis for Research and Applications. *Journal of Climate*, *24*(14), 3624-3648. doi: 10.1175/JCLI-D-11-00015.1

Rino, C. L., Brekke, A., & Baron, M. J. (1977, June). High-resolution auroral zone E region neutral wind and current measurements by incoherent scatter radar. , *82*(16), 2295. doi: 10.1029/JA082i016p02295

Schunk, R., & Nagy, A. (2009). *Ionospheres: Physics, Plasma Physics, and Chemistry*. doi: 10.1017/CBO9780511635342

Schunk, R. W., & Walker, J. C. G. (1973, November). Theoretical ion densities in the lower ionosphere. , *21*(11), 1875-1896. doi: 10.1016/0032-0633(73)90118-9

Singh, Y. P., & Badruddin. (2006, April). Statistical considerations in superposed epoch analysis and its applications in space research. *Journal of Atmospheric and Solar-Terrestrial Physics*, *68*(7), 803-813. doi: 10.1016/j.jastp.2006.01.007

Smith, A. K. (2012, November). Global Dynamics of the MLT. *Surveys in Geophysics*, *33*(6), 1177-1230. doi: 10.1007/s10712-012-9196-9

Stober, G., Baumgarten, K., McCormack, J. P., Brown, P., & Czarnecki, J. (2020, October). Comparative study between ground-based observations and NAVGEM-HA analysis data in the mesosphere and lower thermosphere region. *Atmospheric Chemistry & Physics*, *20*(20), 11979-12010. doi: 10.5194/acp-20-11979-2020

Stober, G., Kuchar, A., Pokhotelov, D., Liu, H., Liu, H.-L., Schmidt, H., ... Mitchell, N. (2021, September). Interhemispheric differences of mesosphere-lower thermosphere winds and tides investigated from three whole-atmosphere models and meteor radar observations. *Atmospheric Chemistry & Physics*, *21*(18), 13855-13902. doi: 10.5194/acp-21-13855-2021

Stober, G., Matthias, V., Jacobi, C., Wilhelm, S., Höffner, J., & Chau, J. L. (2017, June). Exceptionally strong summer-like zonal wind reversal in the upper mesosphere during winter 2015/16. *Annales Geophysicae*, *35*(3), 711-720. doi: 10.5194/angeo-35-711-2017

Williams, P. J. S., & Virdi, T. S. (1989, January). EISCAT observations of tidal

789 modes in the lower thermosphere. *Journal of Atmospheric and Terrestrial*
790 *Physics*, *51*(7), 569-577. doi: 10.1016/0021-9169(89)90055-X
791 Wu, Q., Jee, G., Lee, C., Kim, J.-H., Kim, Y. H., Ward, W., & Varney, R. H. (2017,
792 January). First simultaneous multistation observations of the polar cap ther-
793 mospheric winds. *Journal of Geophysical Research (Space Physics)*, *122*(1),
794 907-915. doi: 10.1002/2016JA023560